Designing Z-Scheme rGO-SnS_2 Synergistic Photocatalyst for Photocatalytic Mineralization of Atrazine and 2,4-Dichlorophenoxyacetic Acid and Applying Machine Learning for Predictive Modelling of Photocatalytic Performance

1. Mott-Schottky Analysis

Mott-Schottky (M–S) analysis was used to determine the flat-band potential of SnS_2 and rGO. The electrochemical measurements were performed using a standard three-electrode system, with the modified glassy carbon electrode and an Ag/AgCl reference electrode. A 0.5 M Na_2SO_4 aqueous solution was employed as the supporting electrolyte for all measurements. Initially, 5 mg of SnS_2 and rGO were dispersed in 380 µL of ethanol, followed by the addition of 20 µL of Nafion solution (5 wt%) as a binder. The suspensions were sonicated for 30 minutes for homogeneous dispersion. Then, the prepared inks were drop-cast on the surface of a polished GCE and dried at room temperature. The measurements were conducted at a frequency of 1 kHz with an RMS amplitude of 10 mV. For SnS_2 and rGO, the potential was scanned from –0.8 V to +0.4 V vs. Ag/AgCl, with the applied DC bias set to 0 V.

M-S analysis is generally expressed by [1],

$$\frac{1}{C^2} = \frac{2}{e\varepsilon\varepsilon_0 N_d}\left[\left(V_{fb} - V\right) - K_B\frac{T}{e}\right] \quad \text{.. (Eq..1)}$$

The potential (V) Ag/AgCl reference can be converted into V (RHE) using the following Equation.

All potentials were initially measured versus the Ag/AgCl reference electrode and subsequently converted to the reversible hydrogen electrode (RHE) scale using Equation (2) [2, 3].

$$E_{FB\,(RHE)} = E_{\,(Ag/AgCl)} + 0.197\,V + 0.059 \times pH \quad \text{.. (Eq..2)}$$

Mott–Schottky (M–S) analysis was employed to estimate the flat-band potentials (V_{fb}) of SnS_2 and rGO, as depicted in Fig. S1. The linear regions of the $1/C^2$ versus potential plots were fitted using the Mott–Schottky equation to extract the V_{fb} values. The SnS_2 plot exhibited a positive slope, indicating n-type semiconductor behavior, whereas the negative slope observed for rGO confirms its p-type nature. Based on the converted V_{fb} values and known band gap energies,

the positions of the conduction band (ECB) and valence band (EVB) were calculated. For SnS_2, the ECB and EVB were determined to be 2.018 eV and –0.412 eV, respectively. In the case of rGO, the ECB and EVB were found to be 2.468 eV and –0.142 eV, respectively.

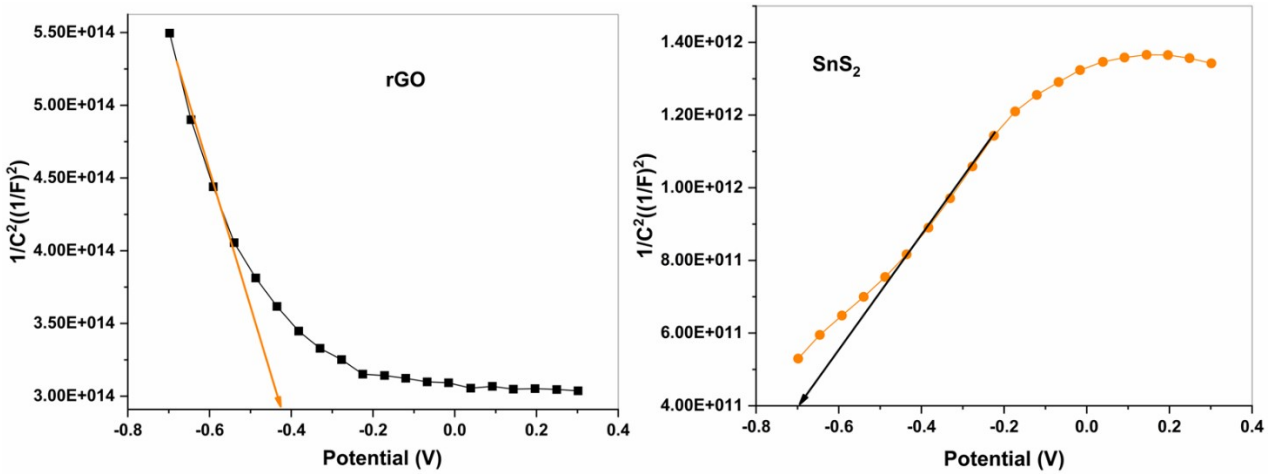

Fig. S1. Mott–Schottky plots of rGO and SnS_2

2. Photocatalytic studies of rGO and rGO-SnS_2 (RS) nanocomposites

The removal of agrochemicals was completed within 3 minutes of exposure to natural sunlight. For additional testing, the test tubes were kept for an extra 15 minutes, showing no significant change in degradation and confirming that 3 minutes is the optimal time for photocatalytic degradation in this experiment. Control studies were performed by keeping one set with the catalyst under dark conditions and another set without the catalyst in light conditions. The results showed no change in the concentration of agrochemicals. Hence, the fact was established that the catalyst in the presence of light causes almost 90 % degradation of the ATZ and 2,4-D.

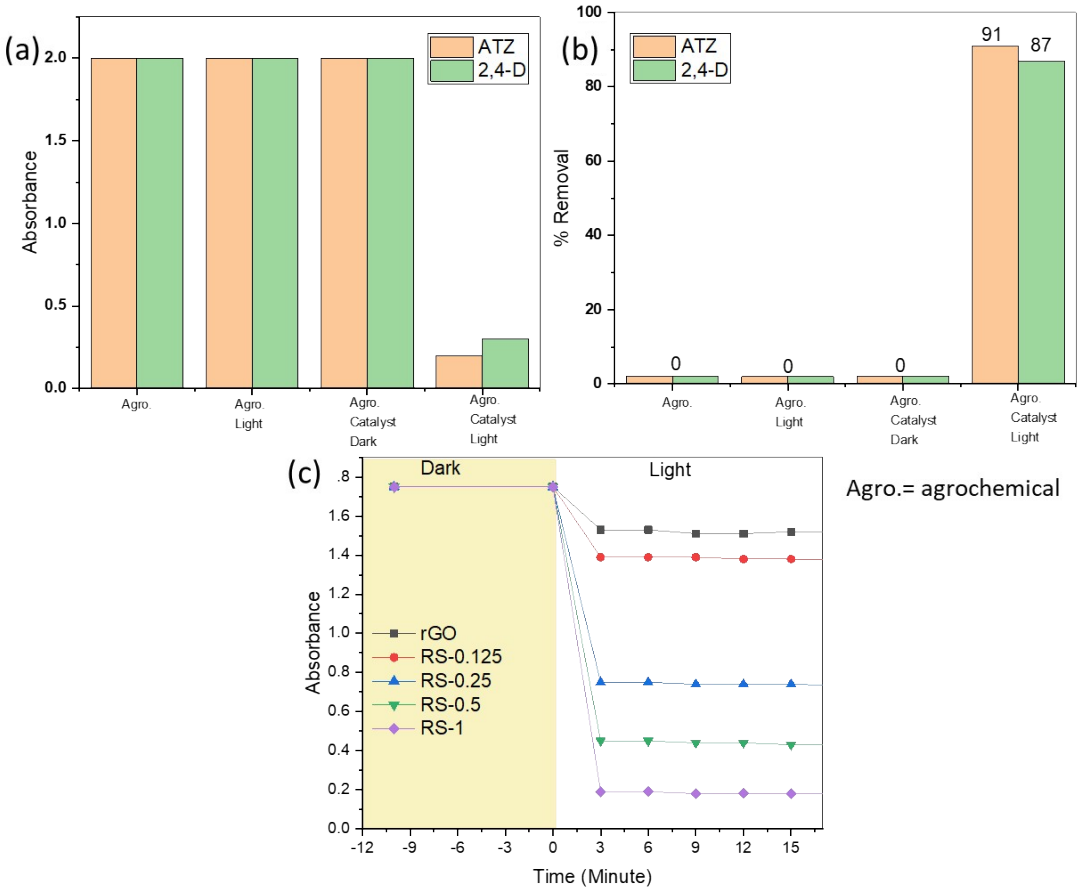

Fig. S2: Control and blank study evaluating the photocatalytic degradation performance of RS nanocomposites against ATZ and 2,4-D (a) Absorbance of agrochemicals under various control conditions, (b) % removal under various control conditions, showing significant degradation only when both catalyst and light are present, (c) Kinetic study showing absorbance vs. time for ATZ under different RS nanocomposites, confirming rapid degradation under light.

3. Identification of agrochemicals using UV-Vis spectroscopy

Identifying degradation products is crucial for understanding the photocatalytic mechanism of ATZ and 2,4-D, and for assessing the potential generation of secondary pollutants to develop a comprehensive mechanism. The degradation products in the supernatant were identified using UV-vis spectroscopy. Fig. S3 confirms the major metabolites of ATZ and 2,4-D, supported by the relevant literature. The absorption spectrum of ATZ and 2,4-D aqueous solution was recorded using UV-vis spectroscopy at a wavelength of 220 and 200 nm, respectively. After degradation in the UV-Vis spectra (Fig. S3 (a-b)) of different RS photocatalysts, the appearance of new peaks and shifts in existing peaks indicate the formation of metabolites and intermediates, as discussed below.

ATZ exhibits two main peaks at 220 nm and 268 nm, as the literature confirms. For rGO, there is no additional peak and change in peak positions at any wavelength, only a decrease in intensity. The appearance of new peaks and shifts in wavelength in the UV-vis spectrum of RS-0.125, RS-0.25, RS-0.5, and RS-1 suggests the formation of new species. In RS-0.125, no new peak appears, but the peak at 268 nm disappears. In RS-0.25, the peak shifts from 220 nm to 225 nm, indicating the transformation of ATZ to Atrazine-desethyl-desisopropyl-2-hydroxy (DEDIHAT) [4]. Additionally, a new peak at 255 nm confirms the formation of Atrazine-2-hydroxy (HAT) [4, 5]. Similarly, for RS-0.5, the intensity at 225 nm and 255 nm decreases, indicating the degradation of DEDIHAT and HAT. The most effective photocatalyst, RS-1, shows the disappearance of all main and newly formed peaks during the degradation process, confirming the complete degradation of ATZ into various metabolites, including DEDIHAT and HAT.

2,4-dichlorophenoxyacetic acid (2,4-D) is a combination of two structures and exhibits 3 main peaks: one corresponding to phenoxyacetic acid (PAA) at 200 nm [6] and two corresponding to 2,4-dichlorophenol (2,4-DCP) at 230 nm and 287 nm [7-9]. rGO shows a decrease in intensity at 220 nm, 230 nm, and 287 nm, with no new peaks or shifts in wavelength. In contrast, all the RS nanocomposites show shifts in peak positions or the appearance of new peaks. In the RS-0.125 nanocomposite, a new peak appeared at 255 nm, which is the formation of any metabolites of 2,4-D. In the RS-0.25 nanocomposite, new peaks appeared at 194 nm, and 211 nm, supporting the formation of hydroquinone (HQ), hydroxycarboxylic acid (HCA), or succinic acid (SA), as confirmed by [10-12]. In the RS-0.5 sample, two new peaks appeared at 225 nm and 252 nm, which are linked to the formation of HQ [10]. HQ, known to have three peaks at 194 nm, 225 nm, and 289 nm, is confirmed by literature [10]. The best photocatalyst, RS-1, shows the disappearance of all previous peaks, with only two small peaks between 260 nm and 271 nm, confirming the formation of phenol (Phe.) [8, 13]. During the degradation of 2,4-D, it transforms into various metabolites, including HCA, SA, HQ, and phenol.

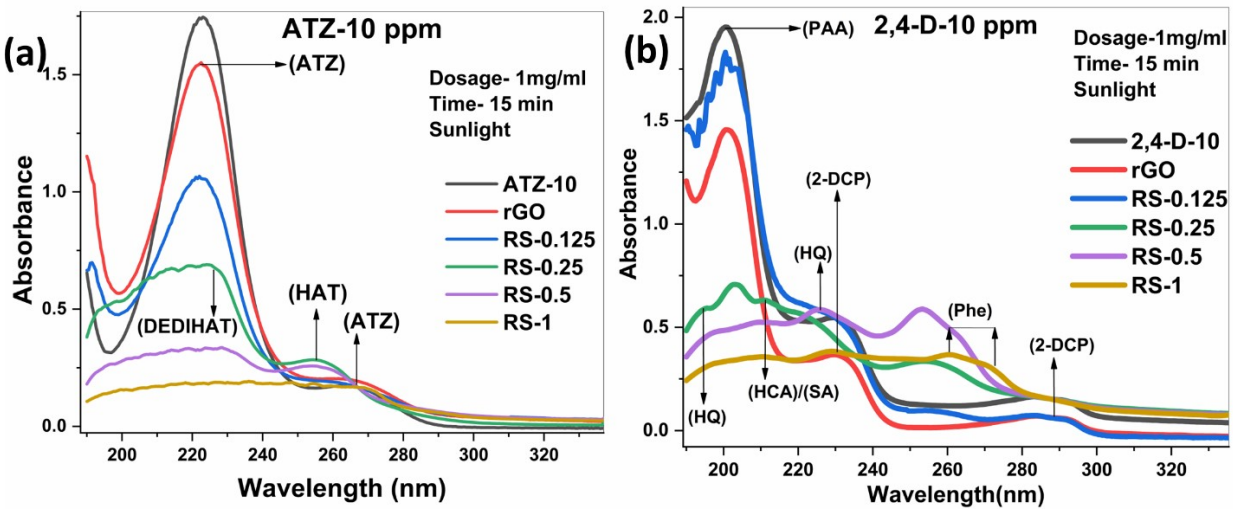

Fig. S3. Degradation of different photocatalysts showing major metabolites of (a) ATZ and (b) 2,4-D confirmed by UV-Vis spectroscopy (Reaction conditions: 10 ppm solution, 1mg/ml, 3 minutes, sunlight)

4. Testing the reliability of the model using an unknown dataset

ANN turns out to be the best-performing model among the three models, SVM, GP, and ANN. To further test the reliability of the model, the dataset was further divided into a training and testing set, still performing satisfactorily for the test set as well. For the training set, the R^2 and MSE are 0.99 and 0.0028, respectively. For the test set, the R^2 and MSE are 0.83 and 0.26, respectively, as depicted in fig. S4. Residual error plots and q-q plots are generated to justify the robustness of the model further. Fig. S4 illustrates the residual error density plot for the training and test sets. Residuals represent the difference between actual and predicted values, are centered near 0, with having mean error and standard deviation close to 0, justifying the model's minimal overall bias. Fig (E) and (F) show the Q-Q plot of the training and test sets, which assess whether the residuals follow a normal distribution or not. The blue dots represent the residuals, and the red line is the ideal normal distribution. A close alignment between blue and red points signifies that the residuals are normally distributed. If the blue points align closely with the red line, it signifies that the residuals are normally distributed. In both training and testing, the residuals are normally distributed, validating the model's accuracy.

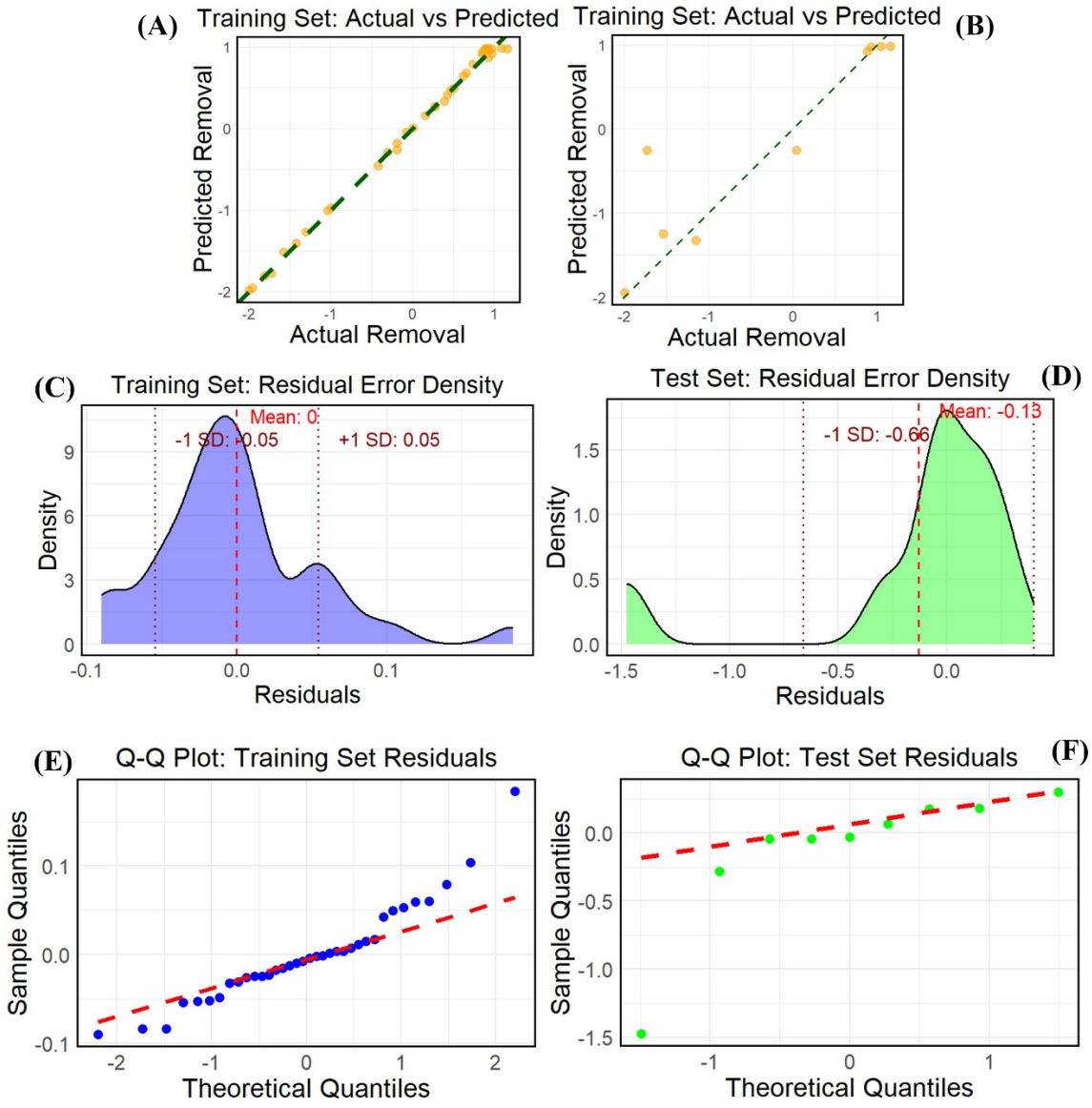

Fig. S4. (A) Plot of ANN model prediction analysis for training set (B) Plot of ANN model prediction analysis for test set (C) Residual error density plot for training set (D) Residual error density plot for training set (E) Q-Q Plot of training set (F) Q-Q Plot for test set

To further assess the reliability and robustness of the model, it was further tested with an unknown data set having similar investigational and output features. The data set included photocatalyst (BZ-10, BZ-5, Biochar, BZ-1, and ZnO), contaminant (ATZ, 2,4-D), Initial concentration of the pollutant, dosage of the catalyst, pH, and time as the investigational features, while removal efficiency was the output feature. The ANN model used in the previous data set was applied to this data set for the prediction analysis of the removal efficiency of the photocatalyst. The model demonstrated tremendous performance, achieving R^2 values of 0.996 and 0.88, and MSE of 0.185 and 0.331, for the training and test sets, respectively. Further

validation by residual error density plot and Q-Q plot, showing normal distribution fit indicating that the model is free of systematic biasness as displayed in fig S5 (C), (D), (E), and (F). Hence, ANN can be a reliable model for the simulation of removal efficiency for unseen data. Following shown are the table (S1) displaying hyperparameter tuning for ANN, SVM and GP model.

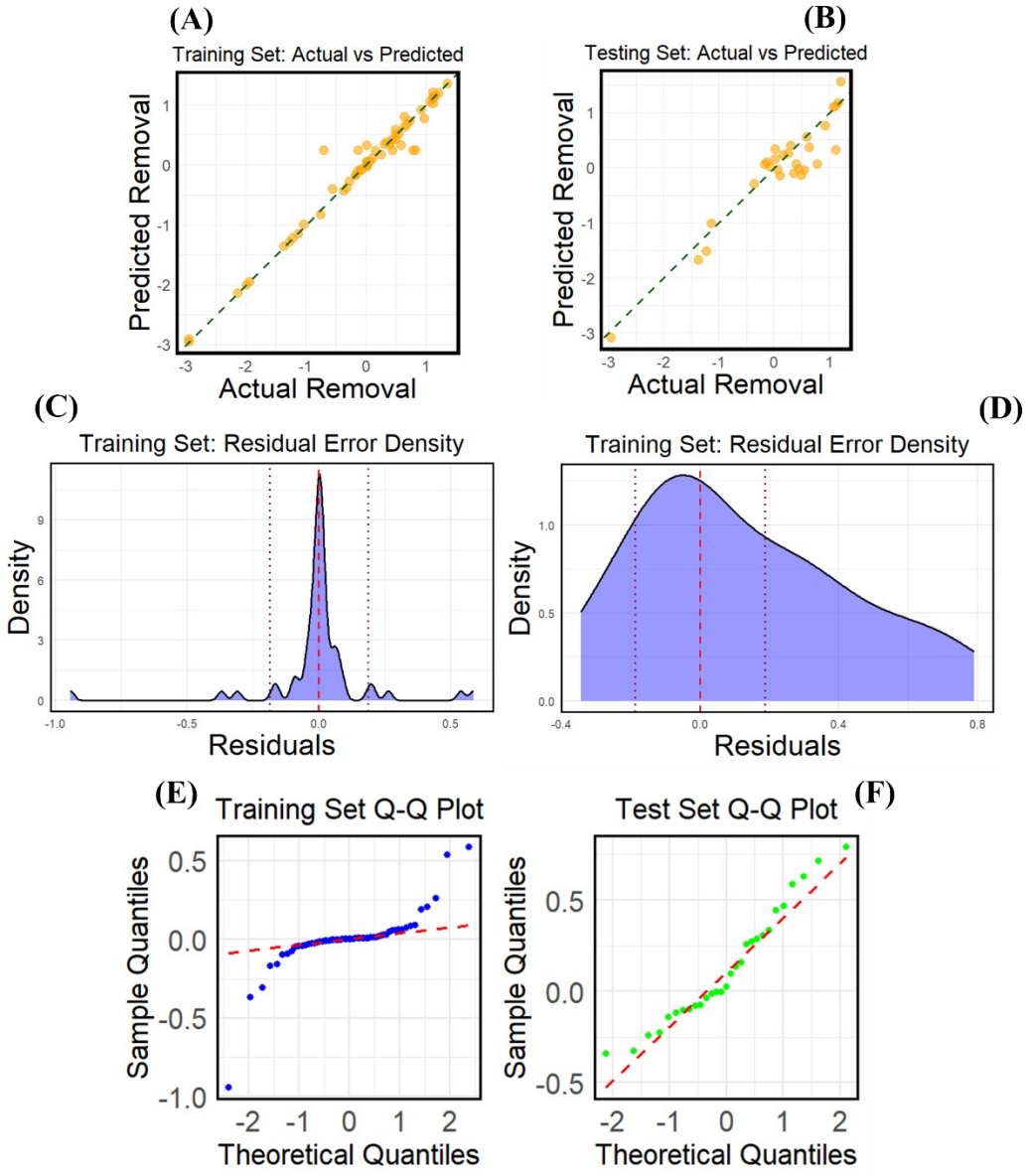

Fig. S5. (A) Plot of ANN model prediction analysis for unknown data set, training set (B) Plot of ANN model prediction analysis for unknown data set, for test set (C) Residual error density plot for training set (D) Residual error density plot for training set (E) Q-Q Plot of training set (F) Q-Q Plot for test set

Table S1: Hyperparameter tuning results for ANN, SVM, and GP models

SVM

sigma	C	RMSE	Rsquared	MAE	RMSESD	RsquaredSD	MAESD	R2_corrected
0.01	1	0.278622	0.540599	0.222348	0.124492	0.286628	0.102471	0.192422
0.01	10	0.275819	0.525842	0.228328	0.114803	0.304443	0.092261	0.36211
0.01	50	0.270307	0.574357	0.226606	0.117357	0.314908	0.098563	0.490139
0.01	100	0.255637	0.625219	0.215317	0.120026	0.326486	0.101043	0.571543
0.05	1	0.266648	0.570897	0.219969	0.124017	0.306242	0.102402	0.344934
0.05	10	0.247439	0.678917	0.208258	0.118089	0.33258	0.099025	0.659663
0.05	50	0.245254	0.703417	0.202917	0.128086	0.320226	0.110236	0.821089
0.05	100	0.26557	0.659538	0.212215	0.13434	0.342771	0.118054	0.827018
0.1	1	0.262261	0.617993	0.221186	0.127486	0.336766	0.109581	0.490419
0.1	10	0.244452	0.704077	0.204732	0.132731	0.339658	0.114544	0.781548
0.1	50	0.279585	0.655246	0.223514	0.15679	0.384685	0.136655	0.826541
0.1	100	0.302711	0.619837	0.246633	0.151588	0.385912	0.132245	0.842758
0.5	1	0.274126	0.620028	0.228094	0.138653	0.349767	0.119703	0.701522
0.5	10	0.361476	0.481146	0.2887	0.171675	0.367839	0.140758	0.738801
0.5	50	0.455618	0.427521	0.360338	0.178349	0.411079	0.148752	0.750094
0.5	100	0.496126	0.435198	0.403225	0.195845	0.397309	0.173663	0.402197

GP

sigma	RMSE	Rsquared	MAE	RMSESD	RsquaredSD	MAESD
0.01	0.295872	0.337031	0.250584	0.018472	0.181033	0.014603
0.12	0.267218	0.405524	0.219989	0.028514	0.16829	0.029952
0.23	0.266034	0.413589	0.219214	0.026627	0.150362	0.029423
0.34	0.27257	0.382424	0.225519	0.025357	0.158304	0.026902
0.45	0.279947	0.342226	0.232354	0.024925	0.166599	0.025756
0.56	0.286208	0.305768	0.238077	0.025043	0.171607	0.025648
0.67	0.29106	0.276569	0.242417	0.025545	0.176058	0.026021
0.78	0.294671	0.254728	0.245585	0.026311	0.181673	0.0266
0.89	0.297292	0.239228	0.248022	0.027251	0.188707	0.027378
1	0.299151	0.228819	0.24982	0.028294	0.1968	0.028213

ANN

layer1	layer2	layer3	decay	MSE	R_squared
4	2	0	0.0001	0.03930421	0.64494459
6	2	0	0.0001	0.0370857	0.66498552
8	2	0	0.0001	0.00201192	0.98182526
4	4	0	0.0001	0.03791453	0.65749829
6	4	0	0.0001	0.04133252	0.62662178
8	4	0	0.0001	0.00083691	0.99243979
4	6	0	0.0001	0.02990112	0.72988761
6	6	0	0.0001	0.0005927	0.96464581
8	6	0	0.0001	0.0010819	0.96022663

4	2	0	0.001	0.04166291	0.62363726
7	2	0	0.001	0.04280682	0.97330367
8	2	0	0.001	0.04300284	0.6115329
4	4	0	0.001	0.03739743	0.66216951
6	4	0	0.001	0.0012663	0.98856081
8	4	0	0.001	0.00080187	0.96275633
4	6	0	0.001	0.04059408	0.63329256
6	6	0	0.001	0.04072576	0.63210298
8	6	0	0.001	0.00158308	0.98569921
4	2	0	0.01	0.04274517	0.61386059
6	2	0	0.01	0.00133073	0.98797886
8	2	0	0.01	0.00230707	0.97915902
4	4	0	0.01	0.03755799	0.66071908
6	4	0	0.01	0.00185693	0.98322534
8	4	0	0.01	0.03605616	0.67428595
4	6	0	0.01	0.03585812	0.67607494
6	6	0	0.01	0.03562966	0.67813868
8	6	0	0.01	0.03915131	0.64632578

References:

1. Mohan Kumar, G., et al. *Effective Modulation of Optical and Photoelectrical Properties of SnS2 Hexagonal Nanoflakes via Zn Incorporation*. Nanomaterials, 2019. **9**, DOI: 10.3390/nano9070924.
2. Chowdhury, D.R., et al., *A robust iron oxyhydroxide water oxidation catalyst operating under near neutral and alkaline conditions.* Journal of Materials Chemistry A, 2016. **4**(10): p. 3655-3660.
3. An, X., K. Li, and J. Tang, *Cu2O/reduced graphene oxide composites for the photocatalytic conversion of CO2.* ChemSusChem, 2014. **7**(4): p. 1086-93.
4. Moreira, A.J., et al., *The process of atrazine degradation, its mechanism, and the formation of metabolites using UV and UV/MW photolysis.* Journal of Photochemistry and Photobiology A: Chemistry, 2017. **347**: p. 160-167.
5. Youssef, L., G. Younes, and R. Al-Oweini, *Photocatalytic degradation of atrazine by heteropolyoxotungstates.* Journal of Taibah University for Science, 2019. **13**(1): p. 274-279.
6. Regulska, E., et al., *Theoretical and experimental studies on alkali metal phenoxyacetates.* Journal of Spectroscopy, 2012. **27**(5-6): p. 321-328.
7. Aifei, Y.I., et al., *Mechanism of 2, 4, 6-Trichlorophenol degradation in microbial fuel cells system with microbe isolated from submarine sediment.* International Journal of Electrochemical Science, 2015. **10**(2): p. 1459-1468.
8. Wei, X., et al., *Understanding electrocatalytic hydrodechlorination of chlorophenols on palladium-modified cathode in aqueous solution.* ACS omega, 2018. **3**(5): p. 5876-5886.
9. Bustos-Ramírez, K., et al., *4-chlorophenol removal from water using graphite and graphene oxides as photocatalysts.* Journal of Environmental Health Science and Engineering, 2015. **13**: p. 1-11.
10. *Hydroquinone.*
11. Koivusalmi, E., *Characterisation and analysis of synthesis mixtures of hydroxy aldehydes, hydroxy carboxylic acids and polyols.* 2001.

12. Thoma, K. and I. Ziegler, *Simultaneous quantification of released succinic acid and a weakly basic drug compound in dissolution media.* Eur J Pharm Biopharm, 1998. **46**(2): p. 183-90.
13. Murillo-Acevedo, Y.S., et al., *The Cramer's rule for the parametrization of phenol and its hydroxylated byproducts: UV spectroscopy vs. high performance liquid chromatography.* Environmental Science and Pollution Research, 2021. **28**: p. 6746-6757.